

Research Article

Optimized Double-Regional Filtering Algorithm on MRI Three-Dimensional Reconstructed Images for the Evaluation of Effects of Delivery on the Pelvis of Primiparas

Qiong Jin ¹, Mian Huang ¹, Jun Lin ¹, Shansan Wu ¹, Zhang Shen ¹,
and Haibing Wang ²

¹Department of Gynecology and Obstetrics, Fuzhou First Hospital, Fuzhou 350009, Fujian, China

²Department of Orthopaedics, Fuzhou First Hospital, Fuzhou 350009, Fujian, China

Correspondence should be addressed to Haibing Wang; fzsdyyy@fjmu.edu.cn

Received 5 April 2021; Revised 6 May 2021; Accepted 17 May 2021; Published 25 May 2021

Academic Editor: Gustavo Ramirez

Copyright © 2021 Qiong Jin et al. This is an open access article distributed under the Creative Commons Attribution License, which permits unrestricted use, distribution, and reproduction in any medium, provided the original work is properly cited.

This study was to explore the denoising and segmentation effect of dual-domain image denoising (DDID) algorithm, and the Galois field (GF) and nonlocal means (NLM) algorithms were introduced for comparative analysis. 40 primiparas in the hospital from January 2018 to January 2020 were divided into an experimental group (caesarean section (CS), group E) and a control group (vaginal delivery (VD), group C). The peak signal-to-noise ratio (PSNR) and segmentation parameters of DDID algorithm were compared with GF algorithm and NLM algorithm. It was found that the DDID showed higher overall accuracy (OA) and lower false positive rate (FPR) and false negative rate (FNR). The PSNR of DDID was higher than the other two algorithms. GF algorithm showed the highest edge retention index (ERI). The incidence of pelvic organ prolapse (POP) in group E and group C was 9/20 (45%) and 5/20 (25%), respectively, with extreme difference ($P < 0.05$). Evaluation of the effects of delivery on the pelvis of primiparas with MRI three-dimensional (3D) reconstructed images based on the optimized DDID showed a superior and stable denoising effect and good segmentation, so it was worthy of clinical promotion and application.

1. Introduction

VD affects the pelvic muscles, nerves, and connective tissues, which may be considered clinically as missing tissue Pelvic Floor (PF) support. It has been learned that VD affects the structure and function of the PF [1]. However, there are few reports on how the vaginal function after pelvic floor function is restored. The environmental factors and VD can affect the pathogenesis of pelvic floor disorders. The PF support and the degree of POP at 9 months are evaluated and compared with the situation at 6 months so as to analyze the biological effects of VD. At present, the possible factors affecting muscles, nerves, and connective tissues include tissue healing during postpartum recovery, menstrual period (the first 8 weeks after delivery), and PF function during postpartum strengthening (the rest duration of one year after delivery). The abdominal pressure and PF support or

symptoms can provide practical and feasible target health management for the prevention of pelvic diseases, with a view to adopting practical preventive measures and strategies [2, 3].

Changes in the PF are affected by the life span of women. Pregnancy and delivery are the main risk factors for PF disorders, and clinical manifestations only occur when the disease is serious. POP is caused by VD and CS. After a VD, 25%–50% of women have mild prolapse, 50% have urinary disorders, and 17% have fecal incontinence in the first year after delivery. Young women show a series of PF symptoms that can affect their quality of life and sexual activity. If the symptoms persist, they are diagnosed with PF disorders based on objective findings, the most common symptoms include POP, stress urinary incontinence (SUI), and fecal urinary incontinence (FUI). Apart from VD, there are few risk factors that can be changed, including obesity. Increased

intra-abdominal pressure (IAP) caused by strenuous work has no obvious correlation with POP [4, 5].

DDID is a nonlinear filter that can maintain smooth edges and reduce noise. The weighted average of the brightness values of surrounding pixels represents the brightness of a certain pixel, and it is based on the Gaussian distribution [6]. Most importantly, the bilateral filtering considers not only the influence of pixel Euclidean distance but also the range radiation difference of the pixel domain. The kernel function of bilateral filtering is a comprehensive result of the spatial domain kernel and the pixel range kernel, in the flat area of the image. The change of pixel value is not very obvious, and the weight of the pixel range is close to 1. In this case, the weight of the spatial domain becomes extremely important, which is equivalent to Gaussian blur. In the edge area of the image, the pixel value changes greatly, and the weight pixel value becomes larger.

Starting from the DDID algorithm, this study discussed the denoising effect of the DDID algorithm on the pelvic MRI image of the primiparas, analyzed the performance of the algorithm, and finally, evaluated the degree of POP of the primiparas. It aimed to provide a theoretical basis for MRI image analysis of the pelvis of the primiparas.

2. Materials and Methods

2.1. Noise Distribution in the MRI Image. The amplitude value of the MRI image is the square root of two Gaussian random variables. The random noise that obeys the Rician distribution instead of the Gaussian noise was introduced in the MRI image in this study. Due to the signal-related nonadditive noise, M was set to as the amplitude of MRI image, and the obeyed distribution expression was shown in the following equation:

$$p(M | S, \sigma) = \frac{M}{\sigma^2} \exp\left(-\frac{(M^2 + S^2)}{2\sigma^2}\right) I_0\left(\frac{MS}{\sigma^2}\right). \quad (1)$$

In the abovementioned equation, p refers to the original image, S is the amplitude of the noise-free image, σ represents the standard deviation of the Gaussian noise in the real image and the virtual image, and I_0 refers to the zero-order Bessel function of the first classification.

2.2. Denoising Principles of DDID Algorithm. Firstly, the original noisy image y and the guided image g were performed with the bilateral filtering through the bilateral filtering kernel function $k_{p,q}$. N_p refers to a window taking the pixel p as center and r as radius. Then, the denoising results could be written as follows:

$$\bar{g}_p = \frac{\sum_{q \in N_p} k_{p,q} g_q}{\sum_{q \in N_p} k_{p,q}}, \quad (2)$$

$$\bar{s}_p = \frac{\sum_{q \in N_p} k_{p,q} y_q}{\sum_{q \in N_p} k_{p,q}}. \quad (3)$$

In the abovementioned two equations, \bar{g}_p, \bar{s}_p are the images in the guide layer and the base layer. For $q \in N_p$, the residual errors at the p point of the noisy image and guide image were windowed using the $k_{p,q}$; then, the short-term Fourier coefficient shrunk. The final results are given as follows:

$$G_{p,f} = \sum_{q \in N_p} e^{-i2\pi(q-p) \cdot (f/2r+1)} k_{p,q} (g_q - \bar{g}_p),$$

$$S_{p,f} = \sum_{q \in N_p} e^{-i2\pi(q-p) \cdot (f/2r+1)} k_{p,q} (y_q - \bar{s}_p), \quad (4)$$

where $S_{p,f}$ was shrunk through the wavelet shrinkage factor $k_{p,f}$ constructed by $G_{p,f}$ to obtain the image for the detail layer as follows:

$$\tilde{S}_p = \frac{1}{|F_p|} \sum_{f \in F_p} K_{p,f} S_{p,f}. \quad (5)$$

In the abovementioned equations, F_p refers to the corresponding frequency distribution matrix of $S_{p,f}$; $|F_p|$ is the number of elements in F_p ; and \tilde{S}_p represents the image of detail layer.

Finally, the image of the base layer was superposed with the image of detail layer to get the final denoising result X .

$$X = \bar{s}_p + \tilde{S}_p. \quad (6)$$

The DDID algorithm can segment the noisy image into the base and detail layer for image enhancement in some specific areas, and multiple iterations delayed the denoising time.

2.3. Denoising Principles of GF and NLM Algorithms. The basic principle of NLM algorithm is defined as follows: it was supposed that there were many similar textures on the same image; then, the noisy area could be replaced with the similar texture area, so as to achieve a better denoising effect without too much loss of details.

If a noisy image was v and the denoising image was \tilde{u} , the gray value of pixel in location x in the \tilde{u} could be calculated with the following equation:

$$\tilde{u}(x) = \sum_{y \in I} w(x, y) v(y). \quad (7)$$

In the equation mentioned above, $w(x, y)$ represents the similarity between pixel point x and y , and its value was determined by the distance $\|V(x) - V(y)\|^2$ between the rectangular neighbor $V(x)$ and $V(y)$ taking x and y as centers, respectively, as follows:

$$w(x, y) = \frac{1}{Z(x)} \exp\left(-\frac{\|V(x) - V(y)\|^2}{h^2}\right),$$

$$\|V(x) - V(y)\|^2 = \frac{1}{d^2} \sum_{z \in Sd} \|(vx + z) - v(y + z)\|^2, \quad (8)$$

$$Z(x) = \sum_y \exp\left(-\frac{\|V(x) - V(y)\|^2}{h^2}\right).$$

In the abovementioned three equations, Z is the normalized coefficient, h refers to the smoothing parameter, and S_d represents the small search window area, which controlled the attenuation degree of the Gaussian function. The larger the h , the smoother the change in the Gaussian function and the higher the denoising level, but the lower the resolution of the image; the smaller the h , the more maintained the edge detail components, but the more the noise points. h should be determined based on the noise level in the image.

The GF algorithm was a local linear model. It was supposed that the linear transformation of equation (9) could be found in the filter window ω_k centered on the pixel k :

$$q_i = a_k I_i + b_k, \forall_i \in \omega_k. \quad (9)$$

In equation (9), I_i is the pixel value of the guide image; ω_k is the filter window centered on the pixel k ; (a_k, b_k) represents the linear coefficient of ω_k ; and q_i refers to the pixel value of the output image. The GF algorithm is shown in Figure 1. To solve (a_k, b_k) , the cost function was introduced according to Figure 1 and equation (2); then, equation (10) could be obtained.

$$(a_k, b_k) = \sum_{i \in \omega_k} ((a_k I_i + b_k - q_i)^2 + \varepsilon a_k^2). \quad (10)$$

In the equation given above, ε is the regularization parameter; the larger the ε , the more obvious the filtering effect; the lower the ε , the better the maintained edge effect. The linear coefficient (a_k, b_k) could be solved with equation (10):

$$a_k = \frac{(1/|\omega|) \sum_{i \in \omega_k} I_i - \mu_k \bar{P}_k}{\sigma_k^2 + \varepsilon}, \quad (11)$$

$$b_k = \bar{P}_k - a_k \mu_k. \quad (12)$$

In equations (11) and (12), μ_k and σ_k^2 represent the mean value and variance of the guide image within ω_k ; $|\omega|$ refers to the number of pixels within ω_k ; and $\bar{P}_k = (1/|\omega|) \sum_{i \in \omega_k} P_i$ refers to the mean value of the input image within the ω_k . Then, the final output image is expressed as follows:

$$q_i = \frac{1}{|\omega|} \sum_{i \in \omega_k} (a_k I_i + b_k) = \bar{a}_i I_i + \bar{b}_i. \quad (13)$$

In equation (13), $\bar{a}_i = (1/|\omega|) \sum_{k \in \omega_k} a_k$; $\bar{b}_i = (1/|\omega|) \sum_{k \in \omega_k} b_k$.

2.4. Research Objects. 40 first-time obstetrics and gynecology patients admitted to the hospital from January 2018 to January 2020 were selected in this study, with the age range of 22–32 years and an average age of 27.25 ± 2.21 years. The inclusion criteria were defined briefly as the normal women who gave birth via the vagina for the first time. The exclusion criteria were determined as follows: people with contraindications to MRI examination (such as patients with pacemaker implantation or claustrophobia) and history of

pelvic surgery. In accordance with the principle of random allocation, 20 women with CS were included in group E , and 20 women with natural delivery were included in group C . This experiment was reviewed and approved by the Ethics Committee of hospital, and all subjects signed the informed consent forms.

2.5. Scanning Plan and Main Point Analysis of the MRI Image Based on the DDID Algorithm. Table 1 provides the scanning plan of MRI images based on the DDID algorithm. A patient was selected to analyze the related MRI effects. As shown in Figure 1, the most commonly used examination method for intrauterine pregnancy was ultrasound examination. MRI examination could display the fetus after the second trimester, the fetal abdominal organs, spine, limbs, and the head clearly. In addition, the attachment position of the placenta in the uterine cavity and internal signals could also be clearly observed.

- (1) Imaging diagnosis points: fetal imaging in the middle and late pregnancy could comprehensively display the development of the fetus. Ultrasound can also dynamically observe the fetal heart movement and find early heart congenital malformations.
- (2) Difference from ectopic pregnancy: the uniformly thinned myometrium could not be found around the fetus for the ectopic pregnancy. As the fetus grows, rupture and emergence of acute abdomen could occur.

2.6. POP Grading. On dynamic MRI images, the bladder neck, cervix extension, and Douglas lowest points were undertaken as indicator points for the anterior, middle, and posterior pelvic cavity, and the pubococcygeal line (PCL) was the reference line from the lower edge of the pubic symphysis to the sacrococcygeal joint. The distance from each indicator point to the PCL under the maximum exertion state of the subject was measured (marked as “+” for a value above the line and marked as “original” for a value below the line). Then, the presence and grading of POP were determined based on the measured distances (as shown in Table 2).

2.7. Statistical Analysis. All data were statistically processed with the SPSS22.0 software. The measurement data were displayed with mean \pm standard deviation, and the t -test was adopted for comparison between groups. The counted data were displayed as the number of cases (percentage), and the chi-square test was employed. $P < 0.05$ indicated the difference was statistically obvious and meaningful.

3. Results

3.1. Comparison on Segmentation Parameters of Pelvic MRI Images of Various Algorithms. The results of analyzing the pelvic MRI image segmentation parameters of different algorithms are shown in Figure 2 and Figure 3. The OA, FPR, and FNR of the DDID algorithm were 0.805, 0.0372, and 0.0382, respectively; those of GF were 0.745, 0.0765, and 0.0745, respectively; and those of NLM were 0.727, 0.1240,

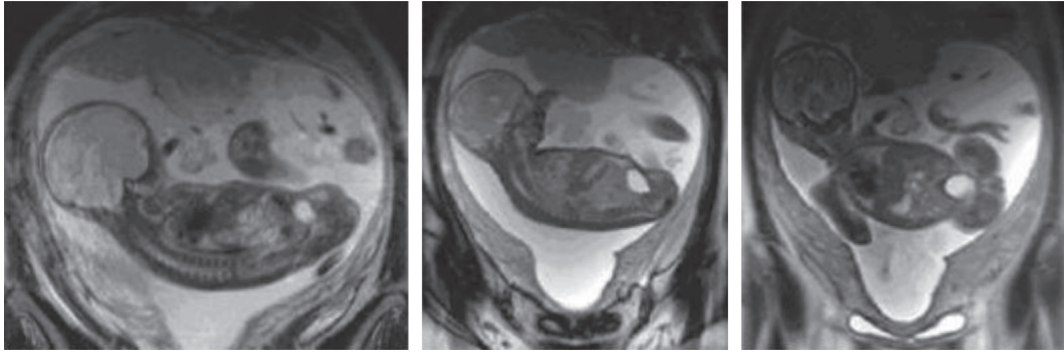


FIGURE 1: MRI images of primiparas (the fetus was formed in the transverse position, facing upward, with the head on the right side. No abnormalities were found in the fetal head, chest, and abdomen. The placenta was located at the fundus of the uterus, lobulated, with uniform signals and a size of about $13 \times 4.9 \times 7.7$ cm).

TABLE 1: The scanning plan and main point analysis of the MRI image.

Sequence	Projection	TR (ms)	Field of view (FOV) (cm)	Slice thickness (mm)	Time of echo (TE) (ms)	Matrix	Number of excitations (NEX)
Fast relaxation fast spin echo (FRFSE)/T2	Sag.ax	5000	24×24	5.0/1.5	100	512×256	4
FRFSE/T2 + fs	cor	5640	24×24	4.0/1.0	102.3	512×224	4
Fast spin echo (FSE)/T1	ax	660	24×24	5.0/1.5	7.6	256×224	4
FSE/T1 + fs	ax	680	24×24	5.0/1.5	7.6	256×224	4
Short TI inversion recovery (STIR)	ax	3620	24×24	5.0/1.5	53.2	256×224	2
3D/CUBE/T2	Sag	3000	24×24	1.6/-0.8	159	288×288	1
3D liver acceleration volume acquisition (3D/LAVA)	Sag.ax	4.2	40×36	4.0/-2.0	2.0	320×192	0.7
Diffusion-weighted imaging (DWI), $b = 1000$	ax.sag	6000	42×42	8.0/2.0	93.1	128×128	8

TABLE 2: Grading of POP.

Grade	Standard
0	All indicator points above or below the PCL line were <1 cm
I	The position of any indicator point of the anterior, middle, and posterior pelvic cavity was 1~3 cm lower than the PCL line
II	The position of any indicator point of the anterior, middle, and posterior pelvic cavity was 3~6 cm lower than the PCL line
III	The position of any indicator point of the anterior, middle, and posterior pelvic cavity was ≥ 6 cm lower than the PCL line

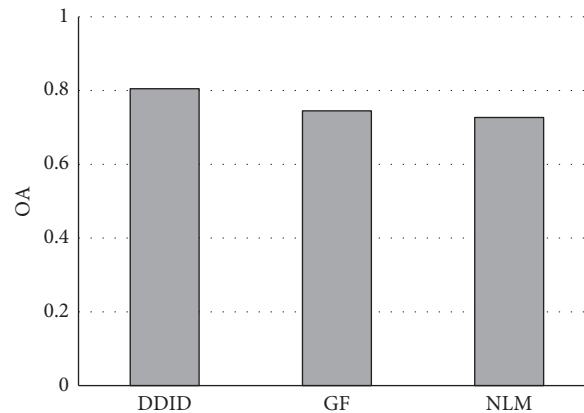


FIGURE 2: Comparison of overall accuracy of different algorithms.

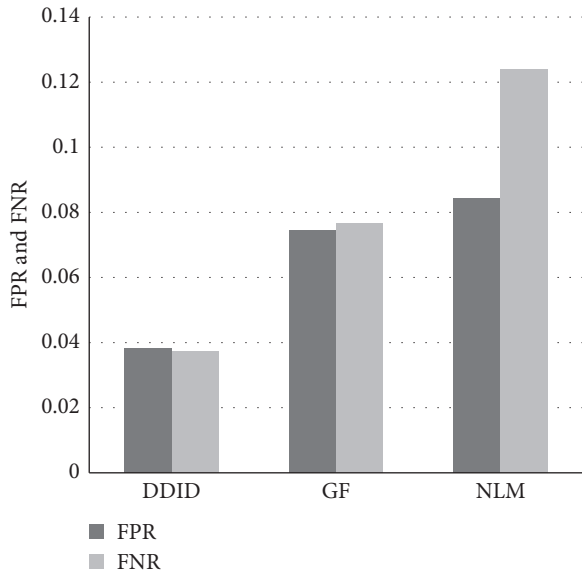


FIGURE 3: Comparison of FPR and FNR values of different algorithms.

and 0.0842, respectively. Thus, the OA of DDID algorithm was higher than the GF and NLM algorithms, and the FPR and FNR of the DDID algorithm were lower than those of the other two algorithms.

3.2. Comparison on Denoising Performance of Pelvic MRI Images of Various Algorithms. The denoising performance comparison of pelvic MRI image segmentation with different algorithms was illustrated in Figure 4. The PSNR and ERI of the DDID algorithm were 27.826 and 0.925, respectively; those of the GF algorithm were 25.454 and 0.968, respectively; and these indicators of NLM were 25.871 and 0.925, respectively. Thus, the PSNR of DDID was higher than that of GF and NLM algorithms. The ERI of the GF algorithm was the highest, followed by the DDID algorithm and the NLM algorithm.

3.3. Analysis on POP of all Patients. It can be concluded from Figure 5 that the organ prolapse of the anterior pelvic cavity was 1.80 cm and 1.64 cm at 6 and 9 months, respectively, that in the middle pelvic cavity at 6 and 9 months was 1.20 cm and 1.28 cm, respectively, and that at 6 months and 9 months in the posterior pelvic cavity was 2.45 cm and 1.18 cm, respectively. Therefore, the results were not statistically different ($P > 0.05$).

3.4. Comparison on MRI Images Denoised with Different Algorithms. The T1w, T2w, and PDw MRI images were selected to analyze and compare the partial enlarged images after denoising. The visual effects of the three MRI images after denoising by the DDID algorithm were obviously better than those of the GF and NLM algorithms. The noise was removed completely by the DDID algorithm, and the image was relatively smooth, effectively avoiding the “blocking

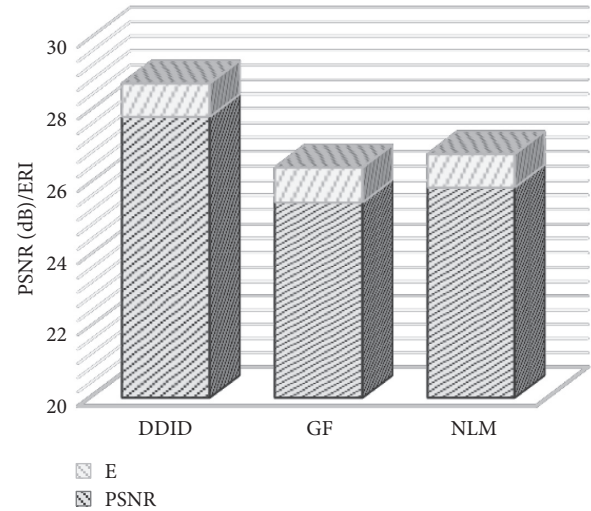


FIGURE 4: Comparison of denoising performances for pelvic MRI image segmentation of different algorithms.

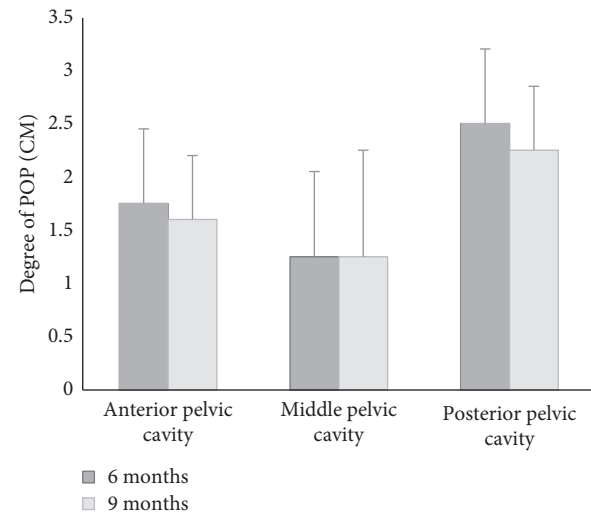


FIGURE 5: POP of patients at 6 months and 9 months.

effect” in the image, which appeared in the MRI image after denoising by the NLM algorithm. In Figure 6, the upper part showed the detailed MRI images of GF algorithm and DDID algorithm for comparison, and the lower part showed the detailed MRI images of NLM algorithm and DDID algorithm for comparison.

3.5. Comparison on the Incidence of POP in Different Groups. The number of POPs for patients in two groups was counted statistically, and the results are given in Figure 7. It revealed that the incidences of POPs in group E and group C were 9/20 (45%) and 5/20 (25%), respectively, so the difference was visible ($P < 0.05$).

4. Discussion

MRI provides a comprehensive understanding of the anatomy and pathology of the pelvis and helps clinical

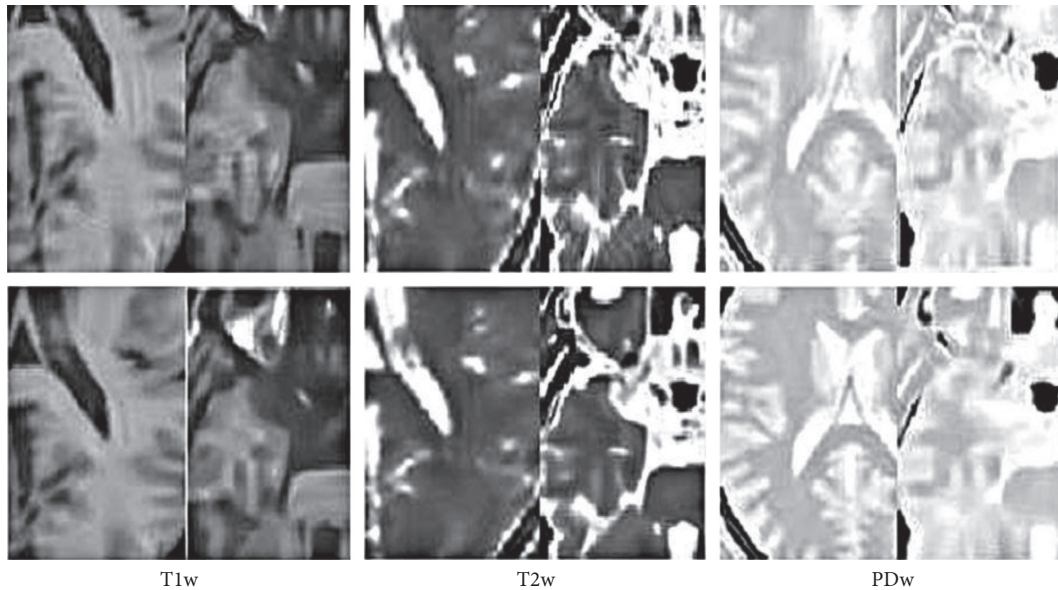


FIGURE 6: Detail comparison diagram of different algorithms. *Note.* The upper three images showed the comparison on the denoising effect of GF and DDID algorithms; and the lower three images showed the comparison on denoising effect of NLM and DDID algorithms.

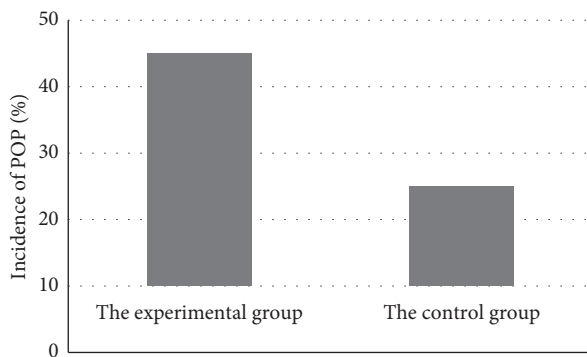


FIGURE 7: The comparison on incidence of POP in two groups.

decisions due to its higher resolution and a larger field of view in contrast to the ultrasound. The sequelae of CS can be accidentally discovered in MRI images of some cases. The methods of MRI imaging research had been described to understand the impacts of physical activity, the support and symptoms of PF muscles, and the environment in which women were located. The abovementioned items are the basic problems of the PF solution. Many of the questions are novel; for example, whether the moderate to vigorous physical activity in the early stages of the postpartum period could bring some risks of pelvic deterioration and PF support as well as PF symptoms for women. The MRI images based on the DDID algorithm predicted that the PF support was more serious and worse. At the same time, it has to study the early change experience of vaginal support for the women after delivery, which can provide important information to guide future prevention work [7–9].

The segmentation parameters and denoising performance on the MRI image of DDID algorithm were compared with those of GF and NLM algorithms. In addition,

the degree of POP with the various algorithms was compared and analyzed further. It was proved that the DDID algorithm was superior to the GF and NLM algorithms in the OA, FPR, and FNR. The PSNR of DDID was higher than the other two algorithms. ERI of GF algorithm was the highest, and that of the other two algorithms was not different greatly. There was no observable different for POP degree of 20 patients at the 9 months and 6 months ($P > 0.05$). The visual effects of the three MRI images after denoising by the DDID algorithm were obviously better than those of the GF and NLM algorithms, which was in consistency with the results of Ai and Ren [10]. The noise was removed completely by the DDID algorithm, and the image was relatively smooth, effectively avoiding the “blocking effect” in the image, which appeared in the MRI image after denoising by the NLM algorithm.

The diseases caused by PF dysfunction have to be concerned, and the PF assessment and PF damage have been widely reported or speculated. Most women have already suffered varying degrees of trauma to the PF during the delivery. It seems that the assessment of the levator muscle space and the diagnosis of levator injury are more reproducible with the help of imaging. MRI was used to dominate the assessment of the PF. However, it suffers from some effects, including high cost, limited accessibility, lack of dynamic imaging capabilities, and unsuitable for women with IUDs or pacemakers. With the advent of 3D ultrasound imaging, it has become easier to study the levator gap. In addition to its low cost, easy access and real-time recording of the dynamic changes of the PF make it possible.

The modern 3D ultrasound systems realize the tomographic diagnosis of levator muscle damage caused by transurethral incision (TUI), which is probably the easiest current technology to repeat, and it has been proven to be comparable to MRI. The 3D ultrasound was adopted in this

study, which found that there were morphological changes of the PF and there were also puborectal avulsion and POP [11].

It was found in this study that the dimension of the hiatus was greater dramatically in group C than in group E; the occurrence of puborectal avulsion was limited to group C, and the incidence of POP was much higher in women who delivered vaginally. The levator ani muscle was lengthened about 25–245%, so the space between the levator muscles was expanded. VD is related to levator muscle injury. It is assumed that the levator muscle avulsion occurs in the fetal head. Whether the defect of the levator ani major muscle is related to the decline of the PF muscle contraction strength and a risk factor for the “expansion” of the levator gap is a mechanism that causes the pelvic organs to sag is not known. Several studies have studied the avulsion of the superior levator muscle; the pelvis is not good to observe the contractility of the floor muscle. It was found that puborectal avulsion only occurred after VD, and the percentage of women after puborectal avulsion was 17.02% of normal VD without equipment assistance, which was consistent with the previously published data, reporting injury rates ranging from 13.3% to 38.5%. It is assumed that the female urethral bladder is supported by the side of the urethra and vagina to maintain the fascia structure, the pubic urethral ligament, and the levator ani muscle. Due to inadequate clinical assessment skills, or insufficiently sensitive imaging methods, the diagnosis of fascial defects is still considered a challenge. It was hoped to believe that the 12 cases of postpartum women with cystocele may be due to weakness or trauma caused by the levator ani muscle or fascial structure. Further research will have an important impact on the imaging performance of fascial abnormalities. Several limitations of this study were mentioned. Because it did not get the volume dataset grouping before and after the ultrasound delivery, the perinatal changes of individual patients cannot be analyzed. An examination was performed in the early postpartum period, which meant that some changes in patients may be reversed, such as those due to transient neuropathy. Therefore, long-term follow-up observations were needed to establish their true significance and resuscitation changes.

5. Conclusions

The denoising effect of the DDID algorithm was evaluated in this study on the MRI images of the pelvis of the primiparas. It was found that the denoising effect of the DDID algorithm was better than that of GF algorithm and NLM algorithm. Then, the degree and incidence of POP of the primiparas were analyzed, which showed that there was no obvious statistical difference for different algorithms ($P > 0.05$), while in the natural delivery group, it was lower than that of caesarean section women. In summary, the DDID algorithm had an excellent denoising effect and good segmentation performance on MRI images of the primiparas, which was worthy of clinical promotion. However, there were still some limitations in this study. For example, the calculation process of DDID algorithm was relatively complicated, which should be continued to be optimized in future work.

Data Availability

No data were used to support this study.

Conflicts of Interest

The authors declare that they have no conflicts of interest.

References

- [1] E. Løwenstein, B. Ottesen, and H. Gimbel, “Incidence and lifetime risk of pelvic organ prolapse surgery in Denmark from 1977 to 2009,” *International Urogynecology Journal*, vol. 26, pp. 49–55, 2015.
- [2] K. Van Delft, A. Sultan, R. Thakar, N. Schwertner-Tiepelmann, and K. Kluivers, “The relationship between postpartum levator ani muscle avulsion and signs and symptoms of pelvic floor dysfunction,” *BJOG: An International Journal of Obstetrics & Gynaecology*, vol. 121, no. 9, pp. 1164–1172, 2014.
- [3] J. Rikard-Bell, J. Iyer, and A. Rane, “Perineal outcome and the risk of pelvic floor dysfunction: a cohort study of primiparous women,” *Australian and New Zealand Journal of Obstetrics and Gynaecology*, vol. 54, no. 4, pp. 371–376, 2014.
- [4] S. Brown, D. Gartland, S. Perlen, E. McDonald, and C. MacArthur, “Consultation about urinary and faecal incontinence in the year after childbirth: a cohort study,” *BJOG: An International Journal of Obstetrics & Gynaecology*, vol. 122, no. 7, pp. 954–962, 2015.
- [5] J. A. Ashton-Miller, R. Zielinski, J. M. Miller, and J. O. L. DeLancey, “Validity and reliability of an instrumented speculum designed to minimize the effect of intra-abdominal pressure on the measurement of pelvic floor muscle strength,” *Clinical Biomechanics*, vol. 29, no. 10, pp. 1146–1150, 2014.
- [6] C. M. Durnea, A. S. Khashan, L. C. Kenny, U. A. Durnea, M. M. Smyth, and B. A. O’Reilly, “Prevalence, etiology and risk factors of pelvic organ prolapse in premenopausal primiparous women,” *International Urogynecology Journal*, vol. 25, no. 11, pp. 1463–1470, 2014.
- [7] M. Wielgos, D. Bomba-Opoń, G. H. Breborowicz et al., “Recommendations of the polish society of gynecologists and obstetricians regarding caesarean sections,” *Ginekologia Polska*, vol. 89, no. 11, pp. 644–657, 2018.
- [8] S. L. Sholapurkar, “Etiology of cesarean uterine scar defect (niche): detailed critical analysis of hypotheses and prevention strategies and peritoneal closure debate,” *Journal of Clinical Medicine Research*, vol. 10, no. 3, pp. 166–173, 2018.
- [9] A. D. Karaosmanoglu, A. Güneş, A. Gunes, M. N. Ozmen, and D. Akata, “Anterior uterine wall: normal and abnormal CT and MRI findings after cesarean section,” *Diagnostic and Interventional Radiology*, vol. 24, no. 3, pp. 135–138, 2018.
- [10] L. M. Ai and Y. H. Ren, “Fast denoising method for medical MR image based on dual-domain filtering and guided image filtering,” *Journal of Optoelectronics Laser*, vol. 29, no. 7, pp. 787–796, 2018.
- [11] M. M. A. Zidan, I. A. Hassan, A. M. Elnour et al., “Incidental extraspinal findings in the lumbar spine during magnetic resonance imaging of intervertebral discs,” *Heliyon*, vol. 4, no. 9, Article ID e00803, 2018.